AGU PUBLICATIONS

Journal of Advances in Modeling Earth Systems

RESEARCH ARTICLE
10.1002/2015MS000498

Global-scale convective aggregation: Implications for the Madden-Julian Oscillation

Nathan P. Arnold[1,2] and David A. Randall[1]

[1]Department of Atmospheric Science, Colorado State University, Fort Collins, Colorado, USA, [2]Now at Global Modeling and Assimilation Office, NASA Goddard Space Flight Center, Greenbelt, Maryland, USA

Key Points:
- Nonrotating convective aggregation occurs on scales of ~4000 km
- Aggregation is supported by a cloud-longwave feedback and a shallow circulation.
- The MJO and aggregation both depend on the convective entrainment rate

Correspondence to:
N. P. Arnold,
nathan.arnold@nasa.gov

Citation:
Arnold, N. P., and D. A. Randall (2015), Global-scale convective aggregation: Implications for the Madden-Julian Oscillation, *J. Adv. Model. Earth Syst.*, *7*, 1499–1518, doi:10.1002/2015MS000498.

Received 11 JUN 2015
Accepted 10 SEP 2015
Accepted article online 15 SEP 2015
Published online 12 OCT 2015

Abstract Previous work has shown that convection will self-organize in cloud-system-resolving model simulations of radiative-convective equilibrium, and it has been suggested that the convective envelope of the Madden-Julian oscillation (MJO) may be organized by similar processes on a much larger scale. Here we present support for that hypothesis based on simulations with SP-CAM with globally uniform SST. Without rotation, convection self-organizes into large (~4000 km) clusters surrounded by dry regions, while with Earth-like rotation the model produces a robust MJO. The nonrotating aggregation and MJO are found to have similar budgets of moist static energy, both being supported by diabatic feedbacks, particularly cloud-longwave interaction. Mechanism denial experiments show that longwave heating anomalies associated with high clouds are essential to the nonrotating aggregation, and amplify the MJO. Simulations using the conventional CAM show a weaker MJO and a much weaker tendency for nonrotating aggregation, and both MJO activity and aggregation intensity are found to increase with the entrainment rate in the deep convection parameterization.

1. Introduction

Tropical convection is organized on a wide range of scales, from gregarious cumulus towers to squall lines, cyclones and convectively coupled waves [*Mapes*, 1993; *Kiladis et al*., 2009]. One of the more interesting forms of organization has appeared in cloud-system-resolving model (CSRM) simulations of radiative-convective equilibrium (RCE). Under certain conditions, the simulated system will undergo a spontaneous transition in which randomly distributed convection becomes organized into a single "aggregated" patch. This transition begins as positive feedbacks establish a particularly dry region, which then expands until all moist convection occurs within a single quasi-circular moist region [*Bretherton et al*., 2005; *Wing and Emanuel*, 2014].

A number of physical processes have been identified as contributing to aggregation in CSRMs, though their relative importance seems somewhat model dependent. Many studies suggest that diabatic feedbacks are necessary for aggregation to occur. Some form of cloud-longwave feedback has generally been found to be essential, although the relative importance of high versus low clouds is disputed [*Bretherton et al*., 2005; *Muller and Held*, 2012; *Muller and Bony*, 2015]. Wind-modulated surface fluxes can also assist the aggregation process, with enhanced fluxes in convective regions associated with downdraft gustiness. Some studies find interactive surface fluxes essential [*Bretherton et al*., 2005] while in others they are unnecessary [*Muller and Held*, 2012].

A strong relationship between convection and tropospheric moisture may also be important. *Muller and Bony* [2015] found that aggregation can occur without longwave radiative feedbacks as long as cold pools are inhibited by preventing rain reevaporation at low levels. They argue that there are two dominant pathways to aggregation: one based on radiative feedbacks and a distinct "moisture memory" form of aggregation due to convection-moisture interaction (as proposed by *Craig and Mack* [2013]). Deep precipitating convection can be suppressed by entrainment of dry environmental air, leading to a correlation between convection and tropospheric humidity. It is thought that aggregation can occur when column feedbacks linked to convection tend to amplify humidity variations within the model domain. A more detailed review of convective organization in CSRMs can be found in *Wing and Cronin* [2015].

Convective self-aggregation in idealized simulations is likely related to the theoretical column instabilities that have been identified in previous studies [*Nilsson and Emanuel*, 1999; *Raymond and Zeng*, 2000; *Sobel*

et al., 2007]. While both approaches neatly demonstrate moisture-convection-radiation feedbacks in the absence of large-scale dynamics, the degree to which these results are applicable to the real world is not well understood. Strong mesoscale organization has been observed in tropical field campaigns [e.g., *Houze and Betts*, 1981] and by satellite [e.g., *Tobin et al*., 2012], but it remains unclear how closely these forms of organization resemble the simple quasi-circular systems seen in modeling studies. More generally, aggregation feedbacks play an important role in interactions between clouds, large-scale circulations, and climate, a nexus increasingly recognized as critical [e.g., *Bony et al*., 2015].

The aggregation phenomenon may be particularly relevant to the Madden-Julian oscillation (MJO) [*Madden and Julian*, 1971]. The MJO is the dominant form of tropical intraseasonal variability, but a theory accounting for its major features remains elusive [*Zhang*, 2005; *Zhang et al*., 2013]. The importance of moisture and radiative feedbacks to the MJO is well documented, and it has been argued that the MJO could be a form of convective self-aggregation on an equatorial beta plane, and on a scale much larger than the CSRM studies to date [*Bretherton et al*., 2005]. One leading theoretical paradigm describes the MJO as a "moisture mode," essentially a self-amplifying anomaly of water vapor and precipitation [*Sobel et al*., 2001; *Grabowski and Moncrieff*, 2004; *Bony and Emanuel*, 2005; *Fuchs and Raymond*, 2002; *Raymond and Fuchs*, 2009; *Sugiyama*, 2009; *Sobel and Maloney*, 2012]. Eastward propagation of a moisture mode occurs due to zonal asymmetries in the sources and sinks of moisture, resulting from some combination of geography and equatorial beta-plane dynamics.

While CSRM aggregation studies have typically used limited domains of a few hundred kilometers square, the envelope of enhanced convection associated with the MJO can span 10,000 km in longitude, with equally broad regions of subsidence and suppressed convection. Recent work has extended the RCE paradigm to general circulation models (GCMs), allowing study of convective self-organization at the global scale. The global RCE studies to date have documented instability similar to that seen in CSRMs, with a partitioning into dry and humid regions, albeit on scales of thousands of kilometers. So far, these studies have focused on questions of climate sensitivity and model development, but the configuration appears a promising tool for a wide range of applications [*Held et al*., 2007; *Popke et al*., 2013; *Reed et al*., 2015]. Rotating versions of these globally uniform simulations have developed cyclones and MJO-like phenomena [*Shi and Bretherton*, 2014; *Grabowski*, 2003]. Global RCE simulations have also been performed over land, with aggregation occurring on a hemispheric scale [*Becker and Stevens*, 2014].

Here we present a series of nonrotating simulations using a superparameterized global climate model with globally uniform boundary conditions. Convection is found to self-organize into multithousand kilometer regions of high humidity, surrounded by dry regions of persistent descent. Our goals are, first, to compare the structure and physical balance of these large-scale convective clusters with the mesoscale aggregation seen in CSRMs. And, second, to compare and contrast the nonrotating organization with an MJO-like disturbance that appears in rotating simulations with the same model.

In the interest of clarity, we define an aggregated state as one in which the distribution of column water vapor is bimodal, with two distinct local maxima. Moisture distributions have not been presented in many previous studies of aggregation, so it is unclear if this is a universal property, but at least in our simulations, stronger aggregation is consistently associated with greater bimodality. This definition reflects the theoretical bistability of the tropical atmosphere that is thought to underlie the aggregation process, in which positive feedbacks drive columns toward moist or dry equilibria [e.g., *Raymond and Zeng*, 2000], and may be related to observed bimodality in tropical water vapor [*Zhang et al*., 2003]. We also introduce a nondimensional metric for the intensity of aggregation, σ, defined as the average column saturation fraction in the most humid 20% of columns, minus the average of the driest 20%.

The paper is organized as follows. Model details and experimental setup are described in section 2. In section 3, we document the organization in the basic nonrotating case. Section 4 presents an analysis of the column moist static energy budget, and section 5 explores the sensitivity to model parameters and boundary conditions. In section 6, we restore rotation and compare an MJO-like disturbance with the nonrotating organization. Section 7 contains additional discussion and our conclusions.

2. Model Description and Experimental Setup

Most of the simulations presented here use a superparameterized (SP) version of the NCAR Community Atmosphere Model (CAM3.5), run with the semi-Lagrangian dynamical core, T42 horizontal spectral

resolution, 30 levels, and a 15 min time step. In a superparameterized model, the boundary layer and convection parameterizations are replaced with cloud-system-resolving models (CSRMs) embedded in each GCM grid column, so that convective temperature and humidity tendencies and cloud and rainfall statistics are generated by explicit simulation [*Khairoutdinov and Randall*, 2001; *Grabowski*, 2001]. In this study, the host model is an intermediate release of CAM, with physical parameterizations similar to CAM4.0. This version of SP-CAM is identical to that used by *Andersen and Kuang* [2012] and *Arnold et al*. [2013]. Four additional simulations using the conventional version of CAM3.5 are also shown. The convection scheme in these runs is that of *Zhang and McFarlane* [1995], with a dilute plume modification [*Neale et al*., 2008] and convective momentum transport based on *Richter and Rasch* [2008].

We use SP-CAM primarily because of its realistic simulation of the MJO [*Benedict and Randall*, 2009; *Andersen and Kuang*, 2012], a rare feature among current GCMs [*Lin et al*., 2006; *Hung et al*., 2013]. In this case, the embedded CSRMs are the System for Atmospheric Modeling (SAM) version 6.7.5, run with 32 columns of 4 km width, and oriented north-south in a 2-D "curtain." The CSRM time step is 20 s, and the vertical grid matches the lower 28 levels of the GCM. The CSRMs use a single-moment bulk microphysics scheme, detailed by *Khairoutdinov and Randall* [2003]. Radiative calculations with the CAM radiation scheme are performed at each GCM time step on the CSRM grid. Clouds are diagnosed directly from the CSRM moisture field, avoiding the cloud overlap assumptions required in most global models. Surface fluxes remain calculated on the GCM grid using the large-scale wind field, which eliminates the gustiness feedbacks associated with convective downdrafts. Previous work suggests that gustiness plays only a modest role in MJO dynamics [*Araligidad and Maloney*, 2008; *Riley Dellaripa and Maloney*, 2015], although it may contribute to mesoscale aggregation [*Wing and Emanuel*, 2014].

We perform a set of aquaplanet experiments, all with prescribed globally uniform sea surface temperatures (SST) of 27°C, except where otherwise noted. Insolation is made globally uniform by fixing the solar zenith angle at 50.5° and reducing the solar constant to 650 W/m^2, following the approach of *Bretherton et al.* [2005]. These values were chosen to directly mimic conditions used in a CSRM study of aggregation, which in turn were chosen to reflect average tropical conditions. It should be kept in mind that this leads to global average insolation greater than seen on Earth: 413 W/m^2 versus 340 W/m^2. With fixed surface temperatures, the primary impact will be in slightly higher atmospheric shortwave absorption and reduced global average precipitation. We estimate this reduction at approximately 0.5 mm/d, or 20% of the actual mean precipitation.

Other global RCE studies have used slab oceans with interactive surface temperatures [*Popke et al*., 2013; *Reed et al*., 2015]. Since our focus here is a comparison with the aggregation simulated in CSRMs, which generally have used fixed SST, and with the MJO, which experiences only small temporal variations in SST, we believe the use of prescribed SST is justified.

The self-organization of convection is first explored in nonrotating simulations, in which the effects of rotation are minimized by increasing the length of the sidereal day by a factor of 1000. Initial conditions for the nonrotating runs are created incrementally. First, the temperature and moisture profiles are set to the 5°S–5°N average from a standard aquaplanet run [*Arnold et al*., 2013]. Horizontal winds are initially set to zero, with small (0.001 m/s) white-noise perturbations to break symmetry. The model is run for 5 days, and the global mean profiles are used to initialize a second 5 day run. This is repeated once more, and global mean profiles from the third run are then used to initialize the simulations shown here. This effectively allows the model 15 days to adjust toward an RCE state with minimal impact from aggregation, which is known to affect domain-mean quantities. Day 0 of the simulations shown here begins after this adjustment period. The nonrotating aggregation is compared with an MJO-like phenomenon in rotating simulations, which have a sidereal day of 23.93 h but are otherwise identical to the nonrotating case described above. The rotating simulations are initialized from the same uniform conditions.

3. Nonrotating Convective Organization

We begin by examining the organization of convection in the nonrotating case. Within 20–30 days, the uniform initial state separates into dry and humid regions with a characteristic spatial scale 900 km. This scale was estimated from the *e*-folding of the autocorrelation function of precipitable water, following *Craig and Mack* [2013]. Snapshots of column water vapor are shown in Figure 1, during the early stages of organization (day 10), during the intermediate stages (day 15), and in the final equilibrium state (day 120). Similar to

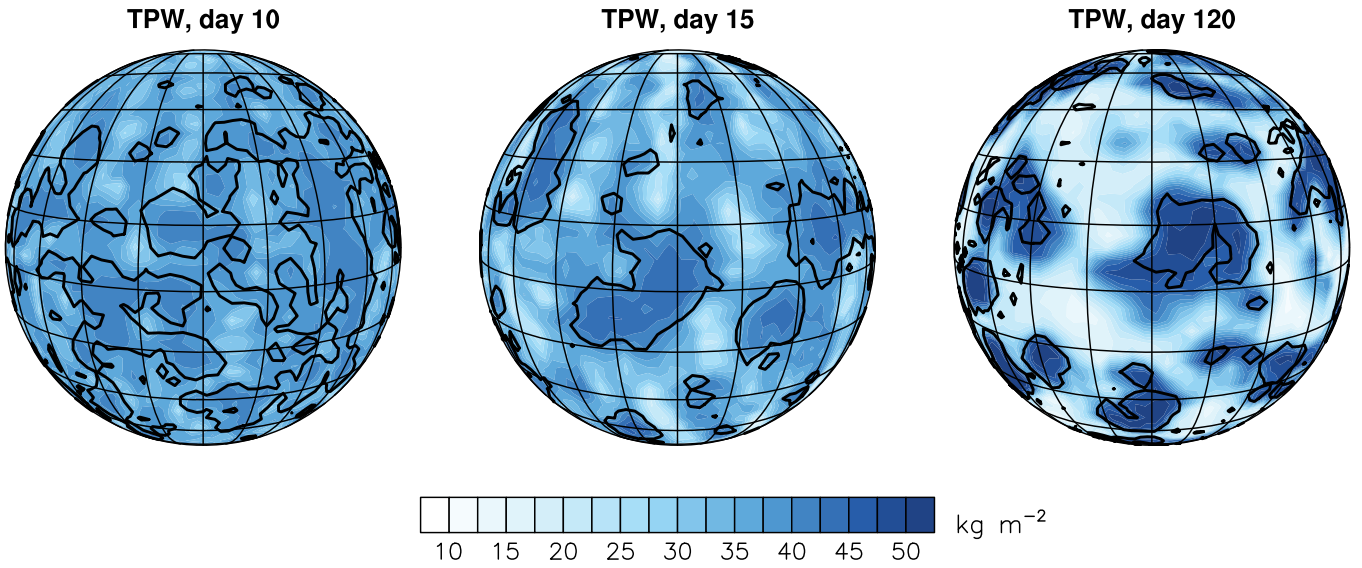

Figure 1. Daily average total precipitable water on days 10, 15, and 120. Black contours indicate where 500 hPa vertical velocities are zero.

aggregation in CSRMs, the humid regions tend to be isolated and quasi circular, while amorphous dry regions fill the remaining domain. The temporal evolution of the total precipitable water distribution is shown in Figure 2. Water vapor content decreases rapidly in the driest regions, while the humid regions moisten more gradually. The minimum precipitable water is established by day 20, while the maximum is not reached until roughly day 90, at which point the precipitable water distribution is statistically steady. Anomalies grow in place and remain largely stationary, drifting only slowly and occasionally merging or breaking apart.

The time scale of aggregation—roughly 20 days—is comparable to that seen in cloud permitting models [*Wing and Emanuel*, 2014], as well as the separate moistening or drying sequences of an MJO event [e.g., *Benedict and Randall*, 2007]. This is unsurprising, given that all of these phenomena are based on moisture-convection feedbacks, and the time scale is consistent with simple scaling estimates [e.g., *Grabowski and Moncrieff*, 2004]. On the other hand, while aggregated convection in CSRMs is typically found in a single cluster, here we find multiple humid regions of somewhat varying shape and scale. Similarities and differences with aggregation in CSRMs are further explored in the next section, which considers the physical processes at work.

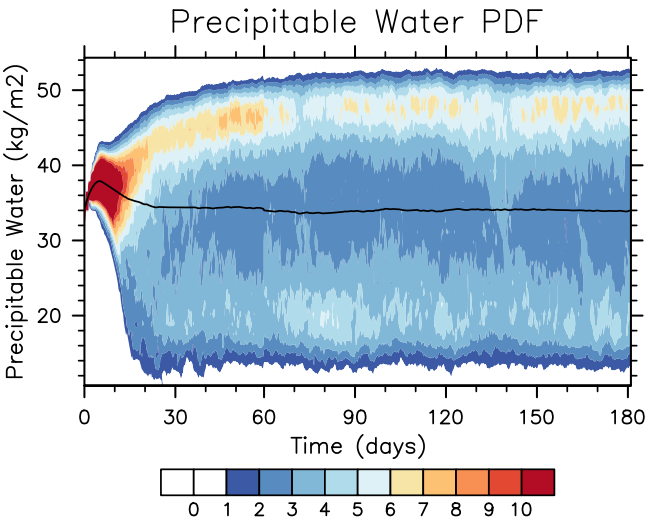

Figure 2. Frequency distribution of precipitable water over time. White curve indicates distribution mean.

Reed et al. [2015] found that global RCE simulations with the conventional CAM5 showed qualitatively different aggregation structure as resolution was varied. *Muller and Held* [2012] raised similar questions about the sensitivity of aggregation to resolution in CSRMs. Here we conduct a limited test of the sensitivity to resolution by running an additional superparameterized simulation with T85 horizontal resolution. We find that the aggregation at T85 looks quite similar to that at T42 (Figure 3). It may be that the superparameterization approach is inherently less sensitive to resolution than a conventional model. It could also be the case that resolution dependence becomes more pronounced at finer grid spacing, where the assumption of scale

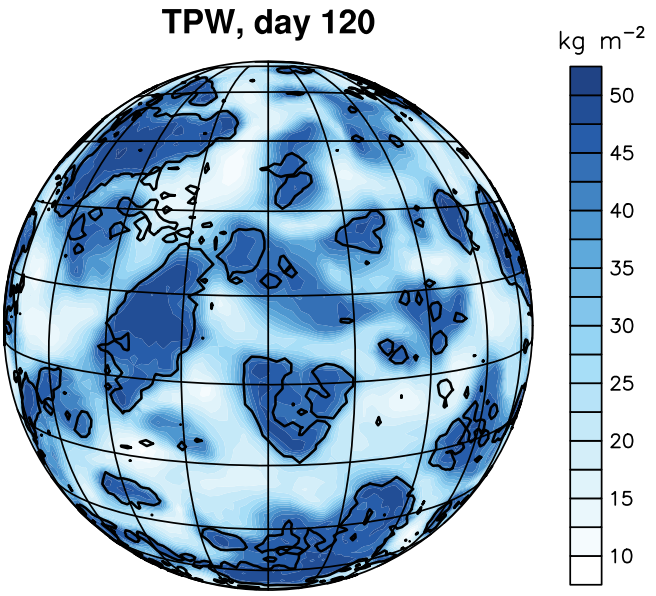

Figure 3. Daily average total precipitable water on day 120, as in Figure 1, for simulation with T85 horizontal resolution.

separation implicit in convection parameterizations is less valid. This question becomes more important as global models move to increasingly higher resolutions, and should be investigated further.

4. The Column Moist Static Energy Budget

In this section, we examine the vertically integrated moist static energy (MSE) budget, with the goals of understanding the physical processes responsible for convective organization and comparing with the processes identified in CSRMs. In the deep tropics, the coriolis force is weak and horizontal temperature anomalies are rapidly smoothed out by gravity waves. Under the resulting weak temperature gradient (WTG) conditions [*Sobel and Bretherton*, 2000], MSE anomalies are essentially water vapor anomalies. In the nonrotating simulations presented here, the Rossby deformation radius is effectively infinite, and WTG conditions prevail across the globe.

Here we use the frozen moist static energy,

$$h = gz + c_p T + L_v q - L_i q_i, \tag{1}$$

where g is gravity, z is geopotential height, c_p is the specific heat capacity, T is temperature, L_v is the vaporization enthalpy, q is specific humidity, L_i is the enthalpy of fusion, and q_i is specific ice content. The frozen moist static energy of convecting air is nearly conserved, including liquid-ice phase changes. As such, convection has little effect on the column MSE,

$$\langle h \rangle = \frac{1}{g} \int_{p(bot)}^{p(top)} h \, dp, \tag{2}$$

which is primarily affected by large-scale advection, surface fluxes, and radiative heating according to

$$\langle \partial_t h \rangle = \langle \vec{u} \cdot \nabla h \rangle + \langle \omega \partial_p h \rangle + \langle LW \rangle + \langle SW \rangle + LH + SH, \tag{3}$$

where angle brackets indicate the vertical integral, $\langle LW \rangle$ and $\langle SW \rangle$ are the vertically integrated longwave and shortwave radiative heating tendencies, and LH and SH are the surface latent and sensible heat fluxes.

Figure 4 gives a sense of the spatial distribution of the vertically integrated budget terms. These are shown as anomalies from the spatial mean, averaged over days 10–30 when dry and humid regions first appear. The shortwave radiative heating and surface sensible heat flux are small fractions of the total tendency and are not shown. Anomalies in the diabatic terms, longwave heating and surface enthalpy fluxes, tend to be in phase with the emerging MSE anomalies, suggesting that the initial organization is supported by diabatic feedbacks. The longwave term in particular has large amplitude and is highly correlated with the developing MSE anomalies. Both advective terms are generally negative in regions of high MSE, although vertical advection tends to be positive on the humid region boundaries.

A more quantitative account of aggregation can be gained by analyzing a budget for the spatial variance of MSE, following *Wing and Emanuel* [2014]. The local tendency of a squared anomaly of column MSE is given by

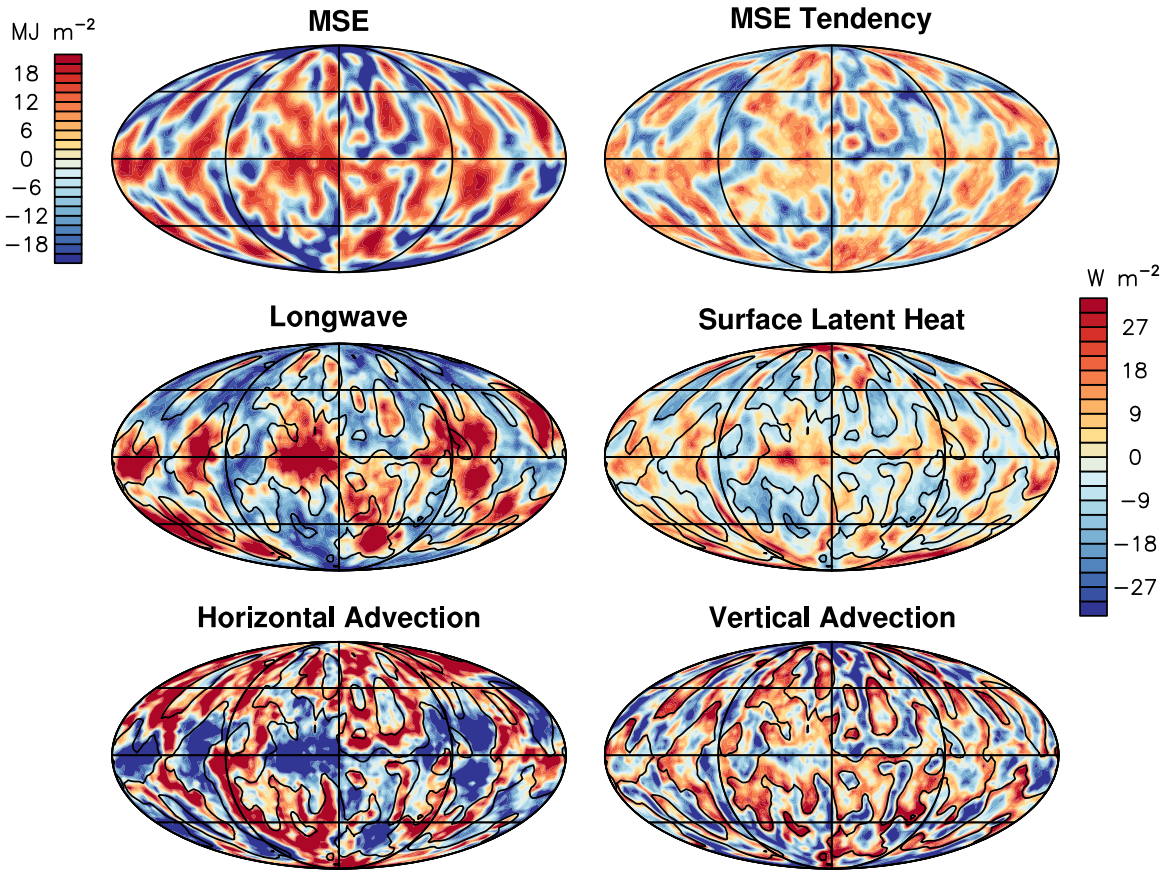

Figure 4. Column moist static energy budget averaged over days 10–30. Black contour indicates 5 MJ m^{-2} MSE. Diabatic terms are positive in the most humid regions, while advective terms tend to be negative.

$$\frac{1}{2}\frac{\partial \langle h\rangle'^2}{\partial t} \approx \langle \vec{u}\cdot\nabla h\rangle'\langle h\rangle' + \langle \omega\partial_p h\rangle'\langle h\rangle' + \langle LW\rangle'\langle h\rangle' + \langle SW\rangle'\langle h\rangle' + LH'\langle h\rangle' + SH'\langle h\rangle', \tag{4}$$

where primes indicate deviations from the spatial mean, and the spatial variance of column MSE is given by the domain average of $\langle h\rangle'^2$. Each product reflects the covariance between MSE sources and MSE anomalies, and thus whether a given budget term contributes to the growth or decay of local MSE anomalies, and at what rate. Averaging each term over the model domain and normalizing by the spatial variance of MSE yields the fractional growth rate of MSE spatial variance due to each term. Without domain averaging, these can be viewed as local contributions to fractional changes in spatial variance.

To distinguish the effects of physical processes in relatively dry versus humid columns, the fractional growth rates associated with each term are binned according to the local column MSE anomaly, yielding growth rate as a function of column MSE and time, shown in Figure 5. Positive growth rates (red shading) imply that anomalies are increasing, i.e., dry regions are becoming drier or humid regions more humid, while negative growth rates imply a reversion to the global mean moisture. This analysis is performed using only columns between 45°S and 45°N in order to minimize the effects of finer grid spacing toward the poles, though we find that the results are qualitatively insensitive to the choice of latitude. The growth rates show, again, that horizontal advection consistently damps MSE anomalies, under humid and dry conditions, and at all stages of aggregation. Vertical advection plays a more dynamic role, strongly opposed to the initial aggregation, but then becomes amplifying, first in the dry regions and then gradually over most of the domain. Eventually, vertical advection overtakes longwave heating as the largest contributor to MSE variance, with the latter remaining dominant only in the core moist regions. The sum of the horizontal and vertical components is strongly negative in the first few days but becomes slightly positive as a steady state is approached. This evolution is similar to that seen by *Wing and Emanuel* [2014].

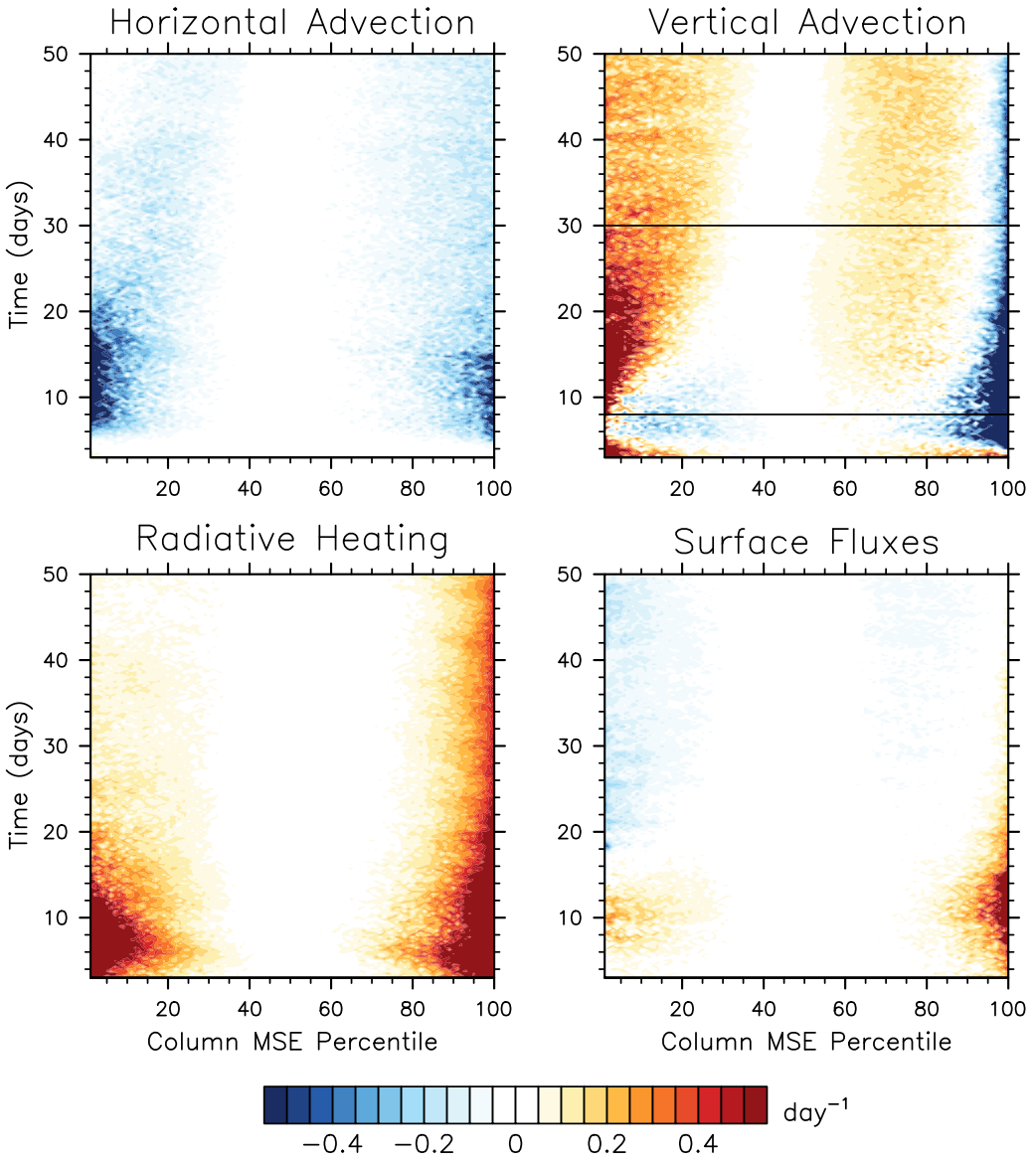

Figure 5. Budget for the spatial variance of MSE over time. Colors indicate the local contributions to the growth of MSE spatial variance.

Anomaly growth rates due to surface enthalpy flux and column radiative heating are both positive in the early stages of organization. Individual components of radiative heating are shown in Figure 6, which indicates the early aggregation is primarily driven by cloud-longwave feedbacks. Clear-sky effects are significantly smaller, and shortwave absorption is smaller still. This suggests that the aggregation in these simulations is not initiated by the clear-sky radiative feedback proposed by *Emanuel et al.* [2014].

The surface evaporation can be broken into components due to spatial anomalies in wind speed, in the undersaturation of surface air, and nonlinear products of the two. Fractional growth rates due to each of these components are shown in Figure 6. The initially positive contribution to MSE anomaly growth is entirely due to wind speed, which is strongly correlated with MSE. As aggregation progresses, horizontal surface winds become weak in the core moist and dry regions and stronger at the boundaries where MSE anomalies are small, reducing its correlation with MSE. At the same time, the drying of boundary layer air in low-MSE regions leads to enhanced fluxes there, compensating for the weaker winds and leading to an overall damping of MSE anomalies. These dynamics closely resemble those reported by *Bretherton et al.* [2005] and *Wing and Emanuel* [2014], with the important difference that in those studies, the wind speed

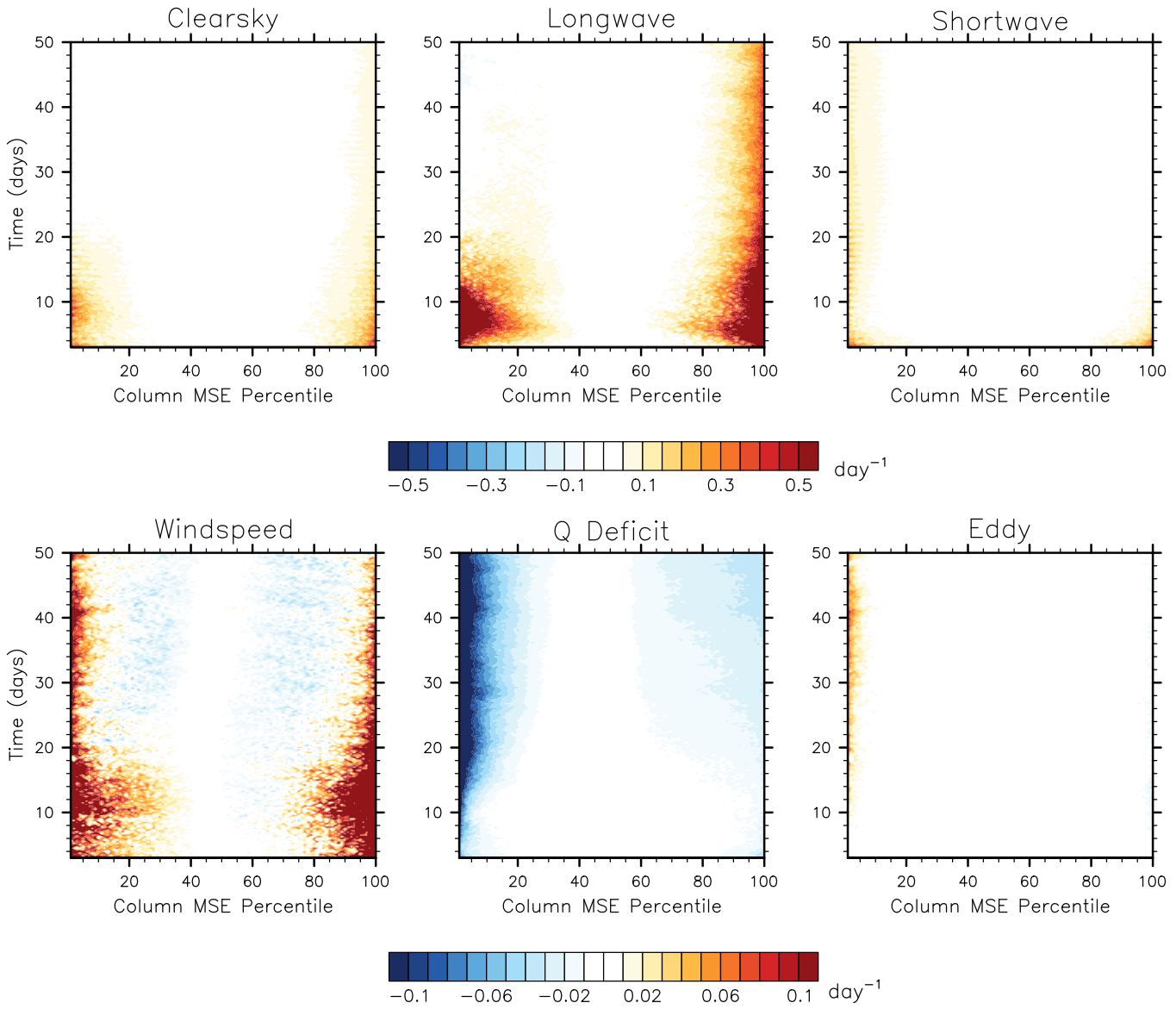

Figure 6. (top) Local contributions to the fractional growth rate of MSE spatial variance due to components of radiative heating. From left to right are total clear-sky, all-sky longwave, and all-sky shortwave, indicating that longwave cloud effects provide most of the initial growth. (bottom) Fractional growth rates due to components of surface latent heat flux. Flux variations due to surface wind speed, surface saturation deficit, and a nonlinear eddy term.

correlation with MSE was thought to be due to downdraft-related gustiness. The sensible heat flux could be similarly decomposed, but due to its smaller magnitude, we neglect to do so here.

We can gain insight into the temporal evolution of vertical advection by examining two time slices. Figure 7 shows vertical profiles of the longwave radiative heating rate, binned by column MSE, and a stream function representing flow between humid and dry regions. The stream function is constructed similar to *Bretherton et al.* [2005] with the exception that we sort individual GCM columns rather than block averages of columns. On day 8, when vertical advection is strongly damping MSE anomalies, we find a relatively top-heavy circulation with maximum vertical velocities near 400 hPa. This top-heavy profile would tend to export MSE from humid regions and import to dry regions, damping MSE anomalies. By day 30, the profiles remain top-heavy only in the most humid columns. In the driest regions, the circulation is strongly bottom-heavy, which would then tend to export MSE and amplify anomalies.

The development of a bottom-heavy circulation can be understood by considering the bottom plots of Figure 7, showing binned profiles of relative humidity (colors) and cloud fraction (contours). By day 30,

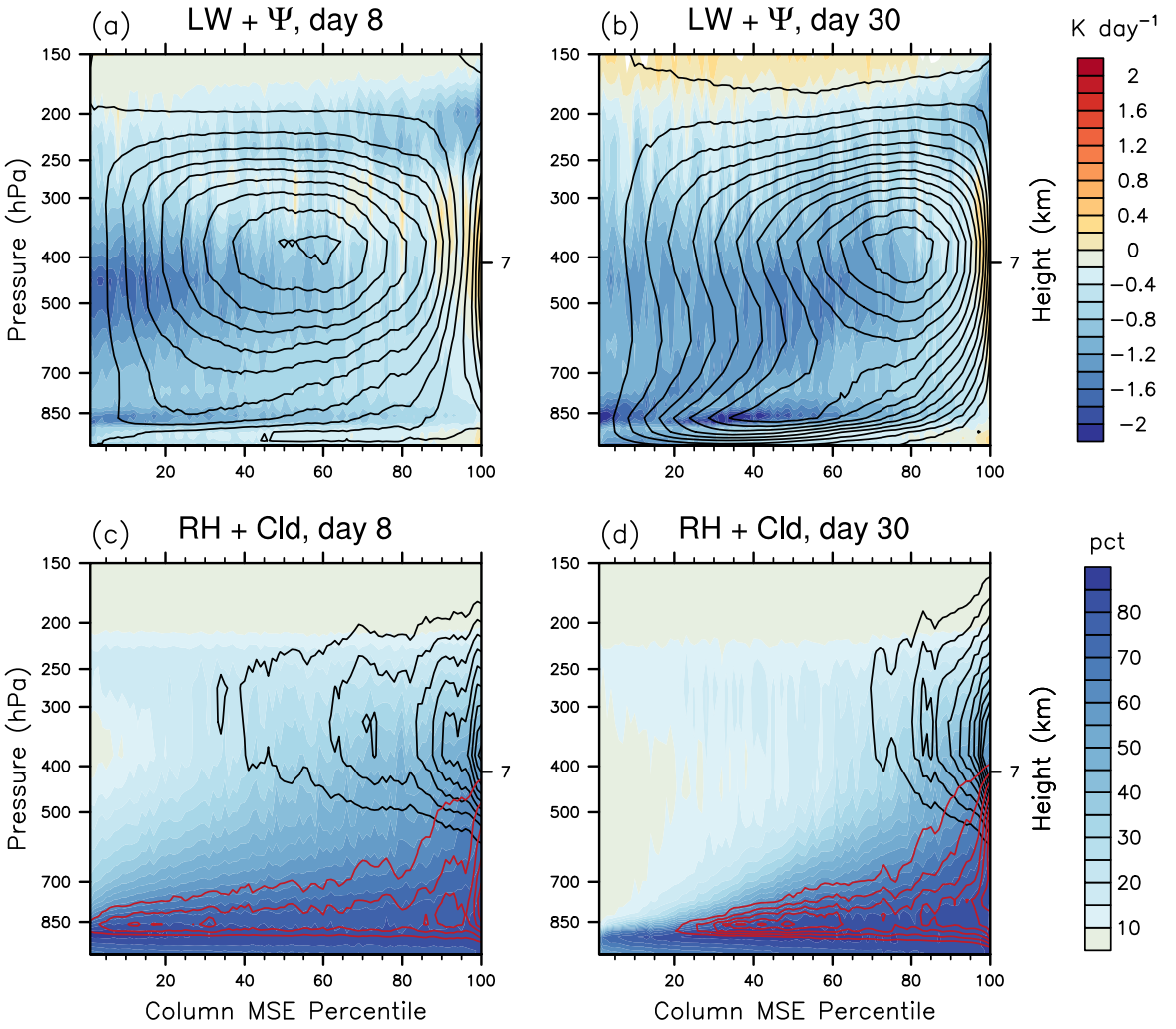

Figure 7. Vertical profiles of (a and b) longwave radiative heating rate and stream function and (c and d) relative humidity and cloud condensate. Contours of cloud ice (black) and liquid (red) condensate use intervals of 0.01 g kg^{-1}.

the low-MSE regions have significantly reduced relative humidity, and lower high cloud fraction. As a consequence, the maximum radiative cooling has shifted to lower levels (Figure 7b). With minimal precipitation, the tropospheric heat balance in these regions is dominated by radiative cooling and adiabatic warming through subsidence. As aggregation progresses, a shift in radiative cooling toward the surface necessitates that the circulation also be bottom-heavy. This is strongly reminiscent of the mesoscale circulation providing up-gradient MSE transport in some studies of CSRM aggregation [*Bretherton et al.*, 2005; *Muller and Held*, 2012; *Muller and Bony*, 2015]. Muller and Held argue this circulation is the primary source of instability in their simulations, although here it seems to provide a secondary positive feedback.

5. Mechanism Denial and Sensitivity Experiments

In this section, we further probe the physical processes maintaining aggregation by varying physical parameters and boundary conditions, and disabling suspected aggregation mechanisms.

5.1. Uniform Longwave Heating and Surface Fluxes

We begin by horizontally homogenizing the longwave heating tendencies, to disable what the MSE budget suggests is the primary feedback amplifying local moisture anomalies. As in the default simulation, radiative calculations are performed on every CSRM column, but here the global horizontal mean longwave tendency

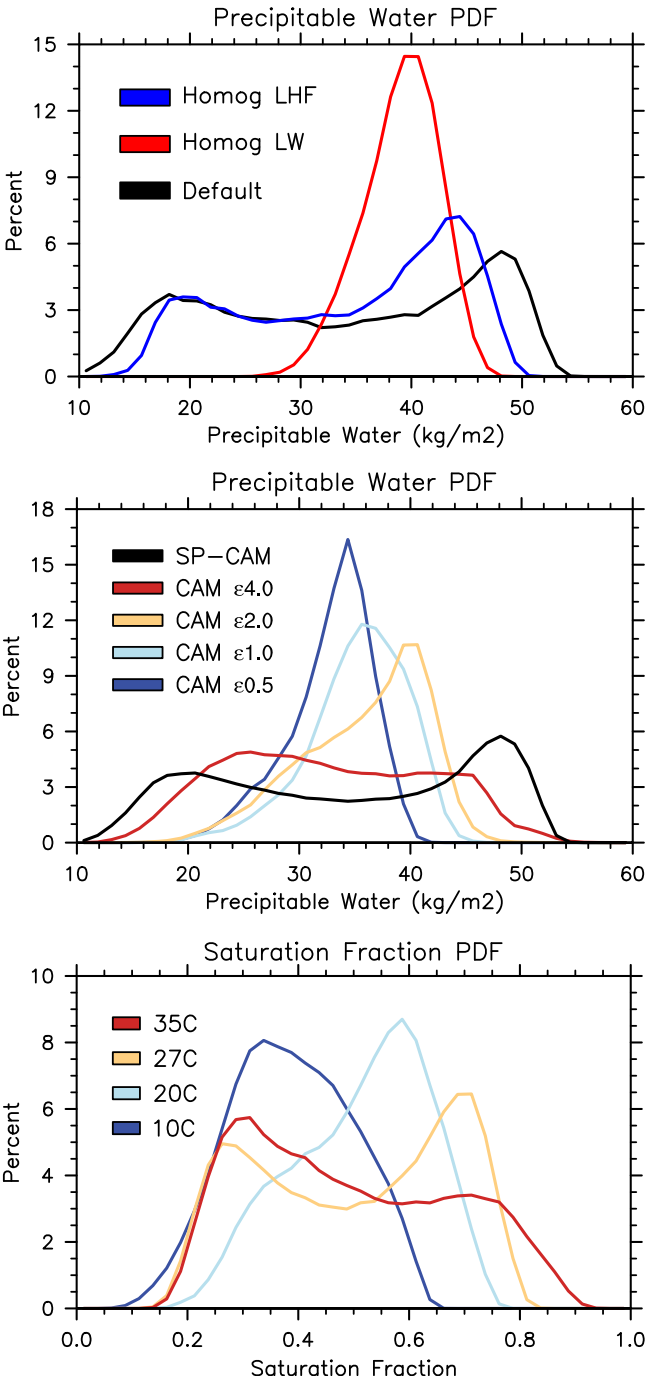

Figure 8. (top) Total precipitable water distribution in the default simulation, and with globally uniform longwave heating or uniform surface fluxes. (middle) Precipitable water in SP-CAM and in CAM with varying convective entrainment rate. (bottom) Column saturation fraction distribution with varying global SST in SP-CAM.

is applied everywhere. Shortwave radiation remains fully interactive. We also conduct a second denial experiment in which the surface enthalpy fluxes are similarly homogenized.

The equilibrium (day 180) distributions of precipitable water from the default, uniform longwave, and uniform surface flux simulations are compared in Figure 8. With homogenized longwave heating, the bimodal moisture distribution collapses into a single peak; aggregation is completely prevented. In contrast, homogenized surface fluxes reduce the minimum and maximum precipitable water, but the bimodal distribution is preserved. The spatial structures of precipitable water are compared with the default case in Figure 9. As implied by the PDFs in Figure 8, eliminating the longwave feedback leads to a much more uniform globe with less pronounced large-scale structure.

Although previous studies have generally found that some form of radiative feedback is essential to aggregation, they have offered differing accounts of its mechanics. *Bretherton et al.* [2005] found that high cirrus clouds reduce radiative cooling in humid columns, while *Wing and Emanuel* [2014] argued that the initial instability is caused by a clear-sky longwave feedback, with cloud-longwave feedbacks becoming important later on. *Muller and Held* [2012] argue that the shallow circulation and up-gradient MSE transport are essential to aggregation, and that strong radiative cooling by low clouds in the dry regions is necessary to support the shallow circulation. To distinguish between these mechanisms, we present two additional simulations in which cloud liquid and cloud ice content are separately set to zero within the radiative calculations. This has the effect of removing local radiative feedbacks due to low and high clouds, respectively.

We find that the intensity of aggregation differs significantly between the two cases. After removing the low cloud radiative feedback, there is little change in the aggregation phenomenology (Figure 10), although the moist regions appear somewhat more interconnected, rather than distinct and quasi circular. The fractional MSE growth rates for each case are also shown, and little difference from the default case is seen when low cloud feedbacks are removed. Early MSE anomaly growth is still driven by a strong longwave

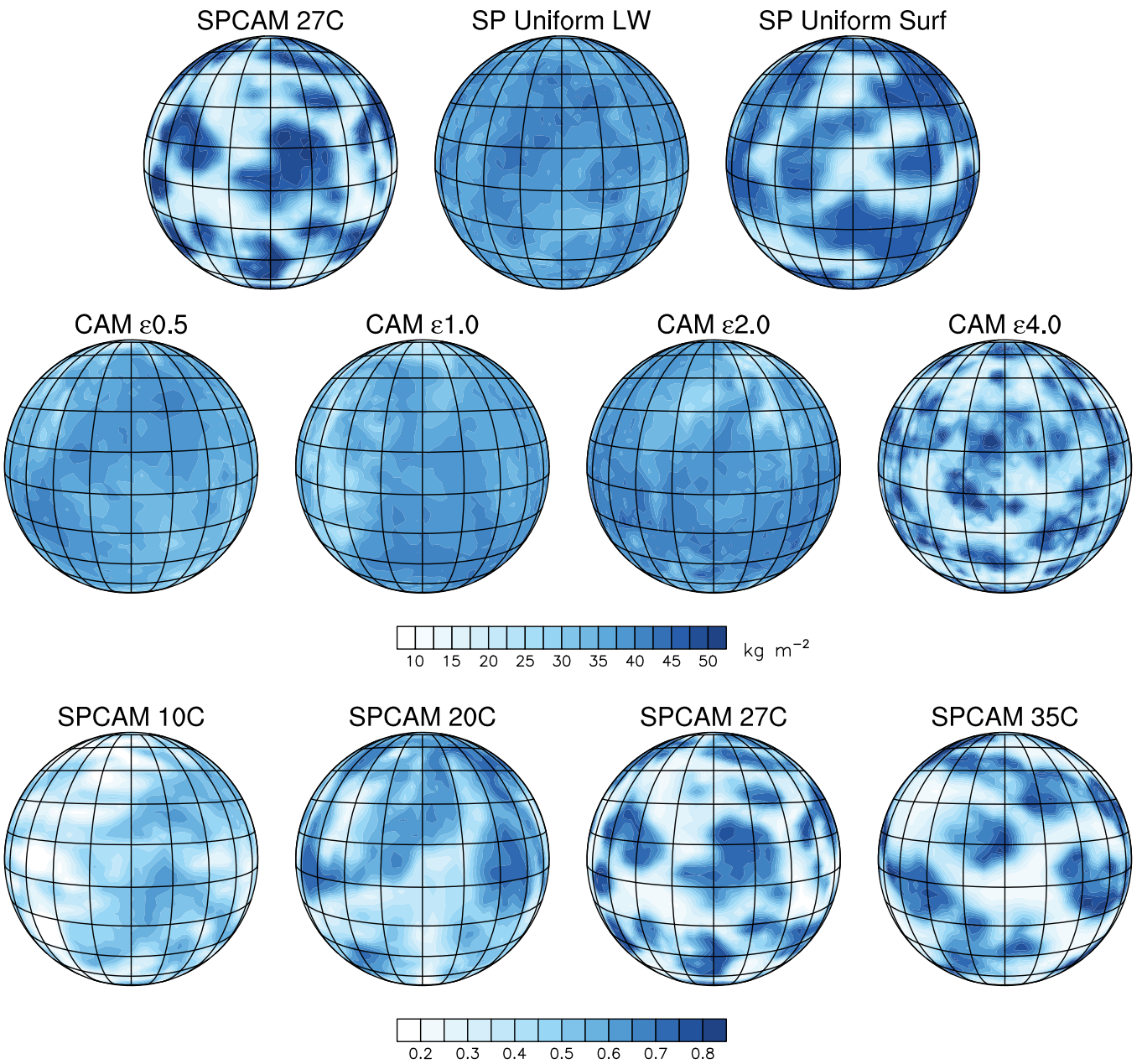

Figure 9. Snapshots of (top and middle) precipitable water and (bottom) column saturation fraction at day 120 of each simulation.

feedback, and vertical advection still amplifies the anomalies in dry regions. This suggests that while low clouds may play a role in reinforcing the shallow up-gradient MSE transport, the circulation is primarily driven by the dry troposphere, which renders the free troposphere largely transparent and allows strong cooling at the top of the comparatively humid boundary layer. In contrast, when the radiative effects of ice clouds are removed, the spatial variation of humidity is noticably weaker. Dry regions are reinforced by vertical advection, which generates larger anomaly growth rates than in the case without liquid clouds.

5.2. Varying the Convective Entrainment Rate

Convection and mid-tropospheric humidity are known to be strongly coupled. This is implied in observations, which show an exponential relationship between precipitation rate and precipitable water [*Bretherton et al.*, 2004], and can be seen directly in cloud permitting model studies [*Derbyshire et al.*, 2004]. A strong coupling between parameterized convection and humidity has also been identified in modeling studies as

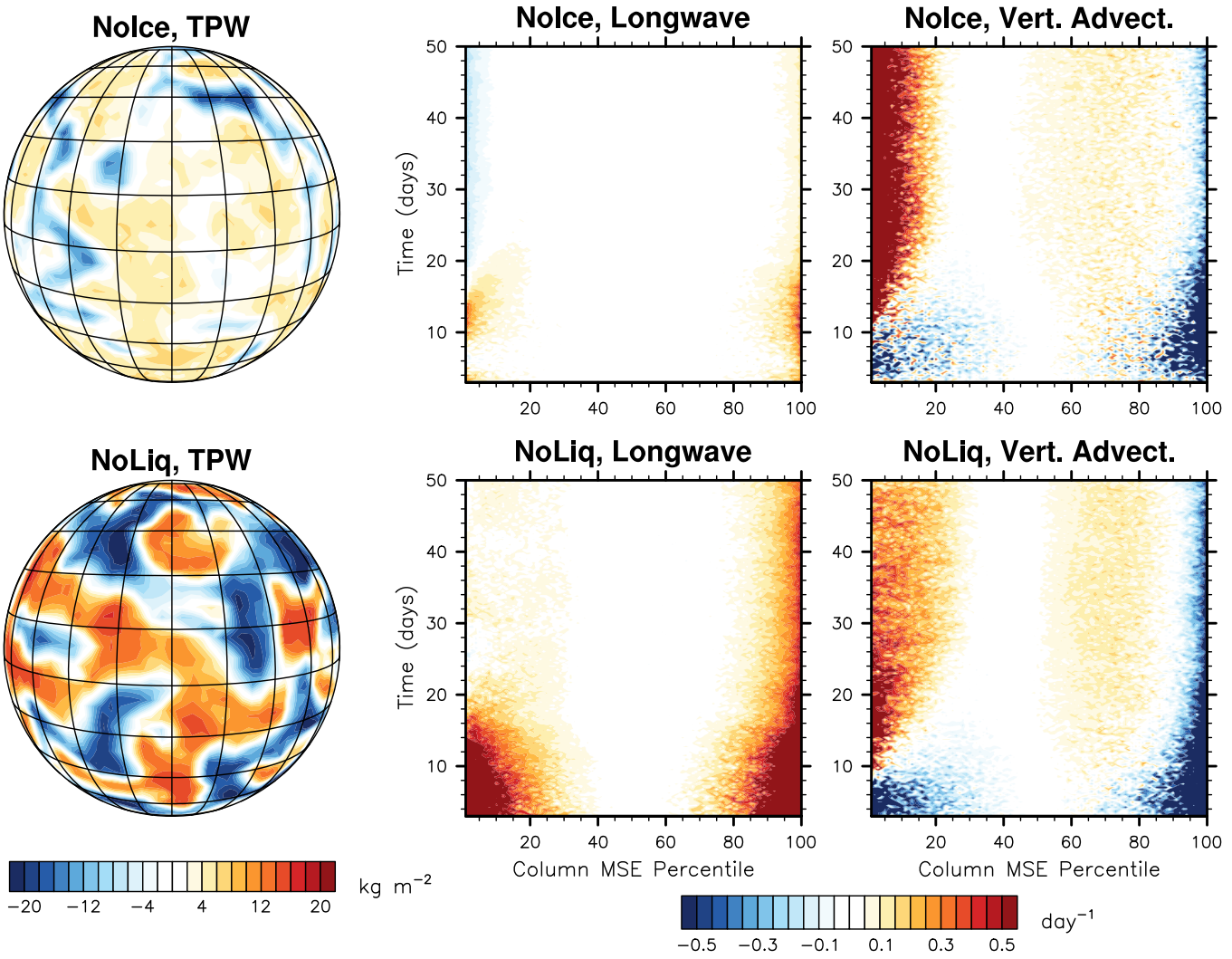

Figure 10. (left) Spatial anomalies in precipitable water on day 90, and (right) local contributions to the growth of MSE spatial variance over time in simulations with no radiative effect from (top) ice clouds and (bottom) liquid clouds. Aggregation is weaker without the ice cloud-longwave feedback.

a prerequisite for realistic MJO simulation [e.g., *Wang and Schlesinger*, 1999; *Thayer-Calder and Randall*, 2009], and simple theoretical models of the MJO often rely on the assumption that precipitation is a strong function of water vapor [e.g., *Fuchs and Raymond*, 2002; *Sobel and Maloney*, 2012].

One approach to increase the sensitivity of convection to mid-tropospheric humidity in GCMs is by increasing the fractional entrainment rate of parameterized convection. In this section, we examine the

Table 1. Global Mean Quantities and Aggregation Intensity, σ, Defined as the Difference in Column Saturation Fraction Between the Most and Least Humid 20% of Columns[a]

Case	Precipitation (mm/d)	OLR (W/m^2)	Net TOA (W/m^2)	CRH	σ
SP 10°C	1.22	226.13	6.5	0.41	0.31
SP 20°C	1.89	242.36	17.1	0.52	0.35
SP 27°C	2.44	255.55	27.9	0.49	0.48
SP 35°C	3.88	266.51	32.5	0.50	0.52
SP uniform LW	2.34	252.17	22.0	0.59	0.20
SP uniform surf	2.31	254.11	25.6	0.54	0.42
CAM ϵ0.5	2.29	251.6	34.4	0.57	0.20
CAM ϵ1.0	2.12	253.0	31.7	0.58	0.23
CAM ϵ2.0	2.16	253.2	32.7	0.59	0.27
CAM ϵ4.0	2.45	257.4	35.8	0.51	0.39

[a]Net TOA values indicate outgoing radiation.

dependence of large-scale organization on entrainment rate in the conventional version of CAM3.5. The fractional entrainment per km in the modified Zhang-McFarlane deep convection scheme is here denoted ϵ, and we vary ϵ from 0.5 to 4.0. We note that ϵ is 1.0 in the default version of CAM5, as part of the Community Earth System Model (CESM1.2).

The precipitable water distributions for SP-CAM and four nonrotating simulations with CAM using varied ϵ are shown in Figure 8. For $\epsilon \leq 1.0$, the distribution has a single narrow peak, indicating that aggregation is effectively nonexistent. As ϵ is increased, the distribution becomes more broad, and for ϵ=4.0, it is clearly bimodal and approaches the distribution seen in SP-CAM. Similar changes are seen in the spatial patterns shown in Figure 9. Increasing ϵ leads to more coherent and more circular humid regions.

5.3. Varying Sea Surface Temperature

Convective self-aggregation in CSRMs has been found to occur more readily at higher temperatures, and may not occur at all below some SST threshold [*Wing and Emanuel*, 2014]. Recent work suggests that aggregation can occur at very low SST [*Abbot*, 2014], but its scale may be temperature dependent [*Wing and Cronin*, 2015]. *Tan et al*. [2015] present observational evidence for increased convection organization with SST. Here we use additional nonrotating simulations with SP-CAM and SST of 10°C, 20°C, and 35°C to probe the temperature dependence of large-scale convective organization.

In comparing the moisture distribution across a wide range of temperatures, it is advantageous to use the column saturation fraction rather than precipitable water. This is defined as the ratio of the vertically integrated specific humidity and the integrated saturation specific humidity. These distributions are shown in Figure 8. There is a general trend for the distributions to become broader with higher SST, implying greater aggregation, with particularly large increases at the humid end of the distribution. At 10°C, there are few GCM columns with saturation fraction above 0.65, but the humidity of the upper percentiles consistently increases with SST. The behavior of the lower percentiles is less consistent, though. The 20°C case is a notable outlier in that its dry tail shifts toward greater saturation, while in the other three cases the relative humidity of the dry tail remains approximately constant with SST. Nevertheless, these distributions are insensitive to the averaging period and seem to reflect a steady equilibrium for each case.

We note that global mean quantities are also sensitive to the above parameters. Global mean precipitation, outgoing longwave radiation (OLR), net top-of-atmosphere outgoing radiation (TOA), and column relative humidity (CRH) are shown in Table 1 along with the aggregation metric, σ. As in studies with CSRMs, we find that OLR increases with aggregation, all else being equal. For example, OLR is larger in SP27C than in SP Uniform Surf or SP Uniform LW, and it increases with ϵ in the CAM experiments. It has been suggested that mesoscale aggregation in nature could play an important climatic role as a "tropical thermostat"; if aggregation increases with surface temperature, the accompanying increase in OLR would provide a negative climate feedback [*Khairoutdinov and Emanuel*, 2010; *Tobin et al*., 2013; *Mauritsen and Stevens*, 2015]. In our simulations the net top-of-atmosphere outgoing radiation increases with aggregation at a lower rate than the OLR, indicating that it is partially offset by decreases in planetary albedo.

6. Adding Rotation Allows an MJO

To compare and contrast the aggregation phenomenon with the Madden-Julian oscillation, we introduce Earth-like rotation to our uniform SST simulations. Boundary conditions, initial conditions, and radiative parameters remain identical. Very similar experiments were conducted by *Grabowski* [2003, 2004] using a different superparameterized model (or Cloud-Resolving Convection Parameterization; CRCP). As in that study, we find a strong MJO-like phenomenon, visible in an unfiltered hovmoeller diagram of equatorial precipitable water and surface precipitation (Figure 11). Water vapor and precipitation anomalies of global scale are seen propagating eastward at 5 m/s. This is against the mean 850 hPa zonal wind, which is 3 m/s easterly. An equatorial wavenumber-frequency spectrum of OLR (Figure 12) shows a strong peak at zonal

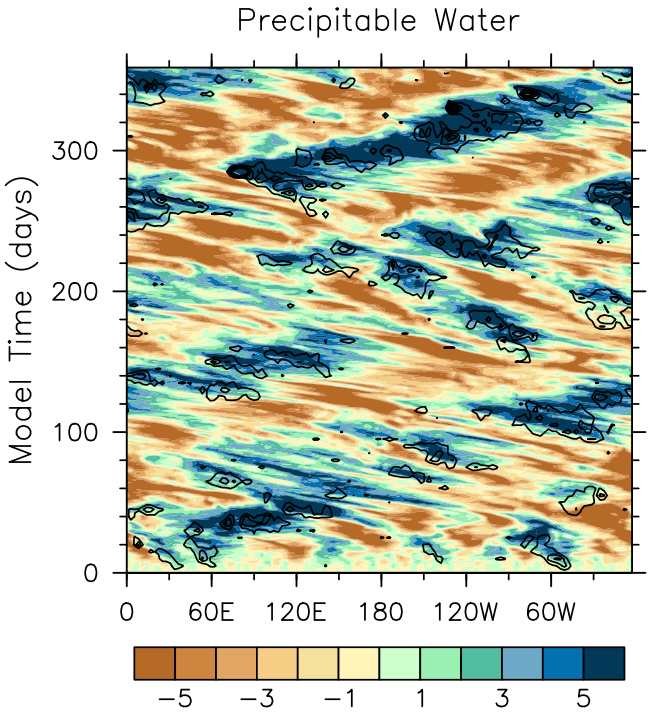

Figure 11. Equatorial (10°S–10°N) precipitable water over time (kg m^{-2}) in a rotating simulation with uniform SST. MJO-like disturbances are visible propagating slowly eastward. Black contours indicate positive precipitation anomalies, in increments of 1 mm d^{-1}.

wavenumber 1 and a period of 60 days. We note that *Shi and Bretherton* [2014] also find an MJO-like spectral peak in globally uniform aquaplanet simulations, although they suggest it may be a convectively coupled Kelvin wave.

We create composites of the MJO using a regression approach based on *Andersen and Kuang* [2012]. Meridionally averaged (5°S–5°N) OLR is filtered to retain zonal wave numbers 1–3 and periods 20–100 days. The filtered OLR time series from each longitude are then concatenated to produce a single reference series. Latitude-longitude and height-longitude fields of interest are similarly concatenated after shifting in longitude so they remain aligned with the OLR series, and then linearly regressed against the reference series. Regression coefficients are scaled by two standard deviations of the reference series, or 16 W/m^2. The composites were compared with an alternative compositing approach based on *Benedict and Randall* [2007], which produced qualitatively similar results.

The resulting composites of precipitation and 200 hPa horizontal wind and geopotential height anomalies are shown in Figure 13a. The quadruple gyre pattern characteristic of the MJO is clearly visible. Vertical profiles of specific humidity anomalies and vertical wind structure are shown in Figure 13b. A low-level moisture anomaly is visible to the east of the precipitation maximum, coincident with low-level moistening by subgrid processes and a shallow vertical circulation (not shown).

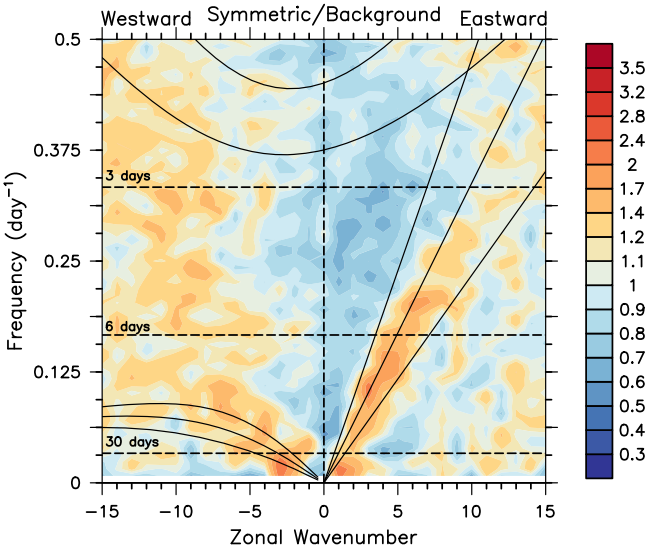

Figure 12. Wave number-frequency spectrum of OLR symmetric across the equator, 15°S–15°N. The ratio of total power over the estimated background spectrum is shown. Dispersion curves use 12, 25, and 50 m equivalent depths.

To relate the MJO to the nonrotating aggregation, we can examine whether they are supported by similar physical processes. To this end, a column moist static energy budget for the composite MJO is shown in Figure 14. The total tendency is quite similar to the MSE anomaly pattern but shifted 90° to the east, indicating eastward propagation, as expected. The longwave term is positive in regions of high MSE, and highly correlated with MSE anomalies near the equator, clearly contributing to MSE anomaly growth. The lack of a visible zonal lag differs from other model studies of the MJO, where equatorial MSE

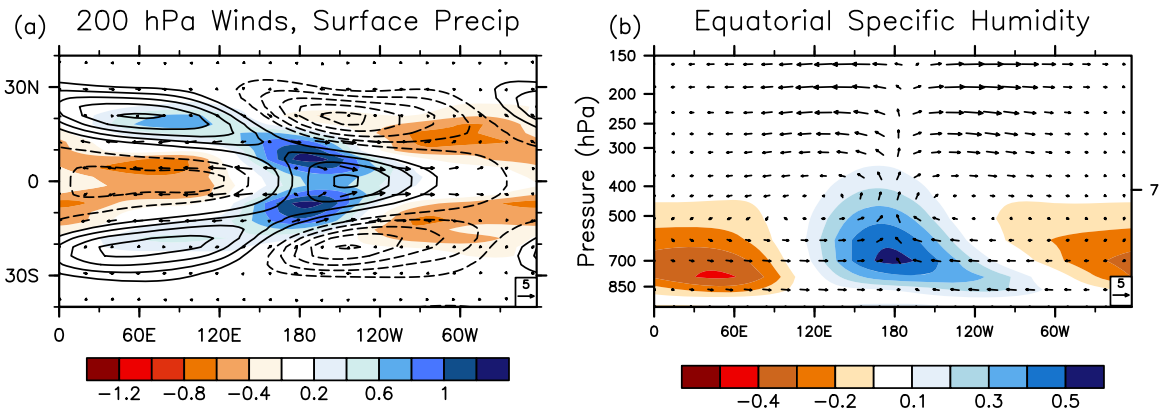

Figure 13. Composites of MJO structure. (a) The surface precipitation (colors; mm d^{-1}) and 200 hPa horizontal wind (vectors) and geopotential height (contours) show a quadrupole gyre pattern. (b) Equatorial specific humidity shows a low-level humid anomaly east of the precipitation maximum that gradually deepens into the mid-troposphere as precipitation intensifies.

anomalies typically lead the longwave term, implying that radiative anomalies slow the MJO's eastward propagation [*Maloney*, 2009; *Andersen and Kuang*, 2012; *Arnold et al.*, 2013; *Crueger and Stevens*, 2015]. This difference may result from the lack of meridional SST gradient here. This would likely reduce the efficiency of meridional MSE advection, which normally contributes to MJO eastward propagation, and may act to "pull" the high MSE region away from the cloud-driven longwave anomalies.

The surface enthalpy fluxes are generally positive to the east and negative to the west of the MSE maximum, and likely contribute to propagation in a manner consistent with the theory of *Emanuel* [1987]. Horizontal advection is the largest sink of MSE in the moist region, acting to balance the large longwave anomalies there, and is consistently positive to the east, contributing to the propagation. The pattern of vertical advection is weakly correlated with MSE, with a strong positive region over the equator to the east of the MSE maximum. This is likely associated with suppressed deep convection and shallow large-scale ascent, and contributes to the MJO's eastward propagation.

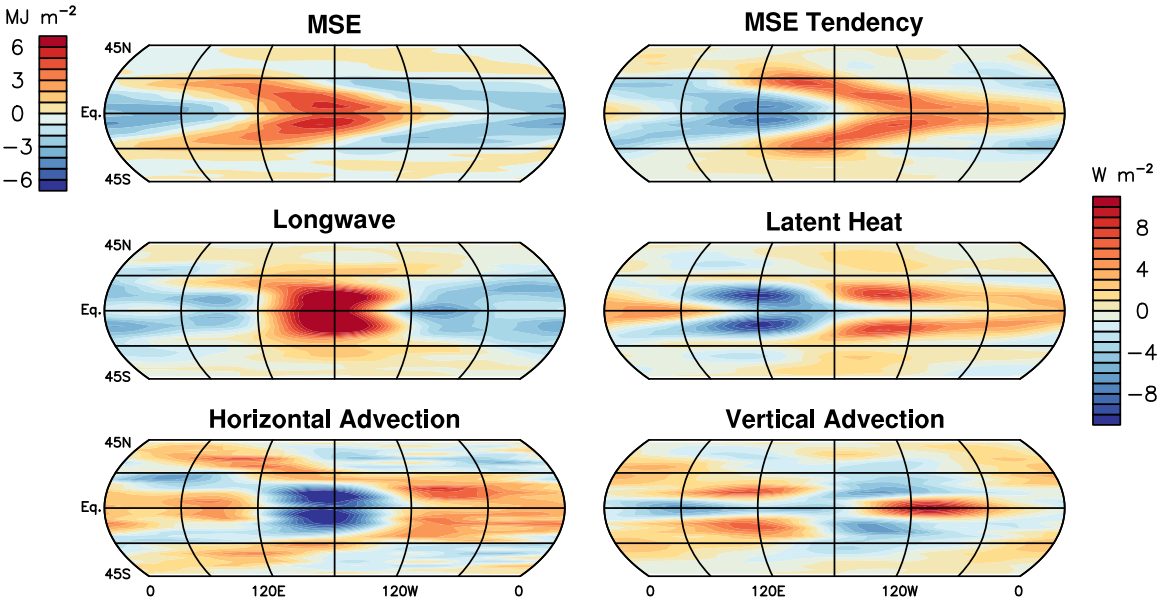

Figure 14. Column moist static energy budget terms for the composite MJO, indicating the importance of interactive longwave.

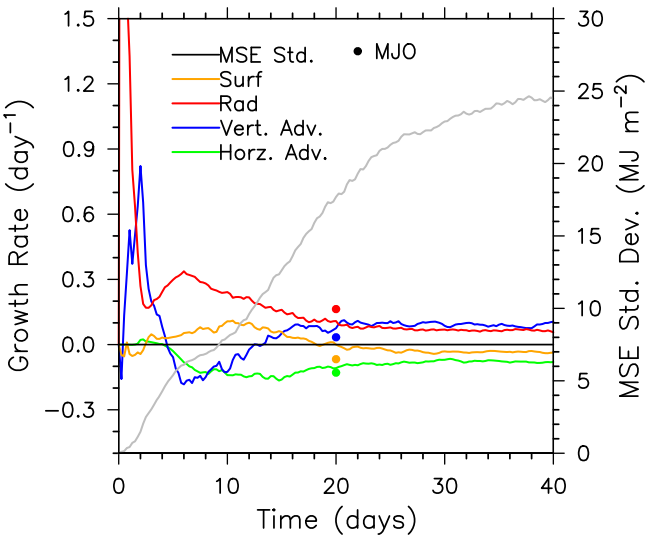

Figure 15. Fractional growth rates of the spatial variance of MSE due to individual budget terms, and the spatial standard deviation of MSE (lines). MSE variance growth rates based on the MJO composite are shown for comparison (points), arbitrarily at day 20.

We can make a limited quantitative comparison with the MSE spatial variance budget for the nonrotating aggregation. The local contributions to MSE spatial variance shown in Figure 5 may be averaged over the domain to provide a single MSE variance growth rate as a function of time, as calculated by *Wing and Emanuel* [2014]. These growth rates are shown as colored curves in Figure 15, along with the spatial standard deviation of MSE (gray curve). As described in section 4, aggregation largely occurs between days 10 and 30, initially driven by radiative feedbacks, which are overtaken by vertical advection around day 20. Horizontal advection consistently damps MSE variance, and surface fluxes initially amplify the variance but become damping by day 20.

For the MJO, we calculate a single time-independent fractional growth rate of MSE variance, F_ϕ, based on the composites shown in Figure 14. This is given by the area integral between 15°S and 15°N,

$$F_\phi = \int_{15S}^{15N} \frac{\langle h \rangle' \cdot \langle \phi \rangle'}{\langle h \rangle' \cdot \langle h \rangle'} dA, \tag{5}$$

where $\langle h \rangle'$ is the composited MSE anomaly, and $\langle \phi \rangle'$ is a given MSE budget term anomaly. Note that this is identical to the MJO growth metrics of *Andersen and Kuang* [2012]. If the MJO composites represent an average MJO, including growth, maintenance, and decay phases, then the time-independent growth rates represent an average of the physical processes contributing to MJO MSE anomalies. These average growth rates are plotted in Figure 15 as filled circles for comparison with the nonrotating variance budget. They show a physical balance qualitatively consistent with the nonrotating aggregation, and generally close to an average of the aggregation growth rates between days 10 and 30. We suspect that if the MJO budget terms were calculated separately for MJO growth versus maintenance periods, they would roughly match the nonrotating aggregation budget during its early (days 10–20) and late (days 20–40) phases.

Previous studies have found that MJO activity is greatly reduced when cloud-radiative feedbacks are removed [*Kim et al.*, 2011] or longwave heating is made zonally uniform [*Andersen and Kuang*, 2012]. Here we test the importance of longwave feedbacks in a uniform SST configuration by globally homogenizing the longwave heating, as done in section 5.1. A slow eastward propagating disturbance is still seen in Hovmoeller plots (Figure 16), and equatorial wavenumber-frequency spectra show an MJO-like peak at zonal wavenumber one. The magnitude of these water vapor anomalies is generally smaller than in the case with interactive longwave, and MJO events occur less frequently. Composites of the moisture and wind fields are qualitatively consistent with those in Figure 13 (not shown), although the precipitation anomaly now has a single maximum centered on the equator. Evidently, interactive longwave is less critical for the model MJO than for nonrotating aggregation, although it significantly amplifies MSE anomalies in both cases.

Finally, we confirm the importance of the convective entrainment rate for MJO variability using a set of rotating simulations with CAM3.5. These employ Earth-like rotation, but are otherwise identical to the nonrotating runs with varying ϵ described in section 5.2. The equatorial wavenumber-frequency spectra of OLR are calculated for years 2–4 of each simulation, and the ratio of raw power to an estimated

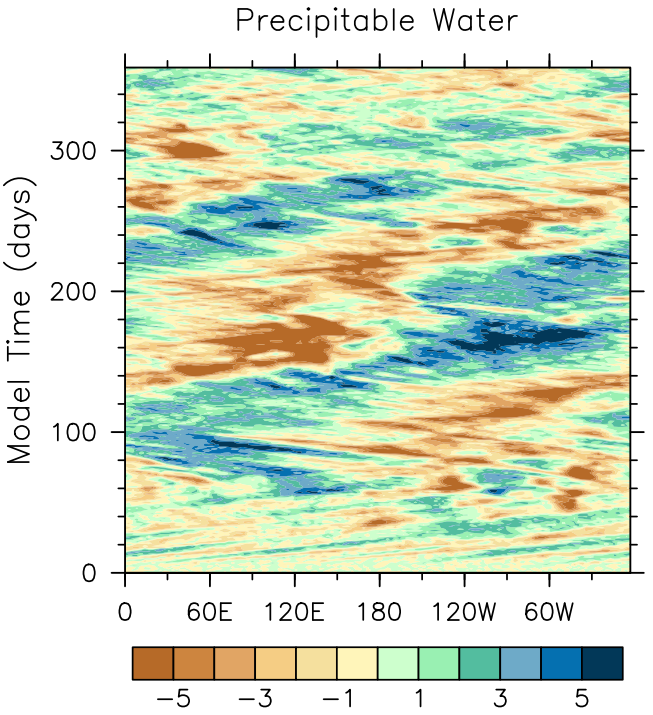

Figure 16. Equatorial precipitable water over time, in a rotating simulation with uniform longwave heating. MJO-like disturbances develop, but are weaker than in the case with longwave feedbacks.

background spectrum is shown in Figure 17. Consistent with previous studies, we find a steady increase in MJO-band variability with increasing convective entrainment, as well as an increase in Kelvin wave variability.

7. Summary and Discussion

We have presented results from nonrotating global simulations with SP-CAM3.5, which exhibit a form of convective self-organization. The global domain was found to partition into distinct dry and humid regions with a characteristic scale of ∼1000 km. This phenomenon is similar to the self-aggregation seen in cloud-system-resolving models (CSRMs), with the primary differences being the larger scale and the appearance of multiple distinct humid regions within the model domain. Process-oriented diagnostics show additional similarities. As with aggregation in CSRMs, the convective organization seen here requires longwave radiative feedbacks. A budget for the spatial variance of column moist static energy indicates a dominant role for cloud-longwave feedbacks in increasing MSE anomalies, and in experiments with globally homogenized longwave heating, aggregation does not occur. Separately eliminating the radiative effects of liquid and ice clouds suggests that it is primarily high clouds that drive the aggregation process, although shallow clouds may play a supporting role. Simulations with homogenized surface fluxes show somewhat weaker aggregation.

As the aggregation becomes established, a shallow large-scale circulation develops which transports MSE up-gradient between dry and humid regions. The MSE spatial variance budget suggests that this is the dominant mechanism maintaining the mature organized state. A similar shallow circulation was also seen in aggregation in CSRMs [*Bretherton et al.*, 2005; *Muller and Held*, 2012]. Sensitivity experiments in which surface temperature is increased suggest the aggregation depends on SST, again similar to the behavior in CSRMs. Aggregation does not occur at all when SST is fixed at 10°C, and occurs only weakly at 20°C. The model simulates systematically higher relative humidity in moist regions and stronger accompanying circulations as SST is increased. Additional simulations with the conventional version of CAM show that aggregation does not occur when the parameterized convective entrainment rate is small, and that the distribution of precipitable water broadens as the entrainment rate is increased.

Aggregation in CSRMs appears to occur via a sharp bifurcation; the domain is clearly aggregated or disaggregated. In contrast, the global-scale organization presented here exhibits a relatively smooth parameter dependence. Varying SST or convective entrainment results in gradual increases in the degree of aggregation (Table 1).

When rotation is restored and boundary conditions remain uniform, the model produces an eastward propagating disturbance with structure similar to the observed Madden-Julian oscillation (MJO). Like the nonrotating aggregation, an MSE budget suggests the model MJO is principally supported by longwave feedbacks, consistent with previous modeling studies [*Andersen and Kuang*, 2012; *Arnold et al.*, 2013; *Hannah and Maloney*, 2014; *Crueger and Stevens*, 2015] and observations [*Sobel et al.*, 2014]. When longwave heating is made globally uniform, the MJO-like variability is significantly reduced, although it does not

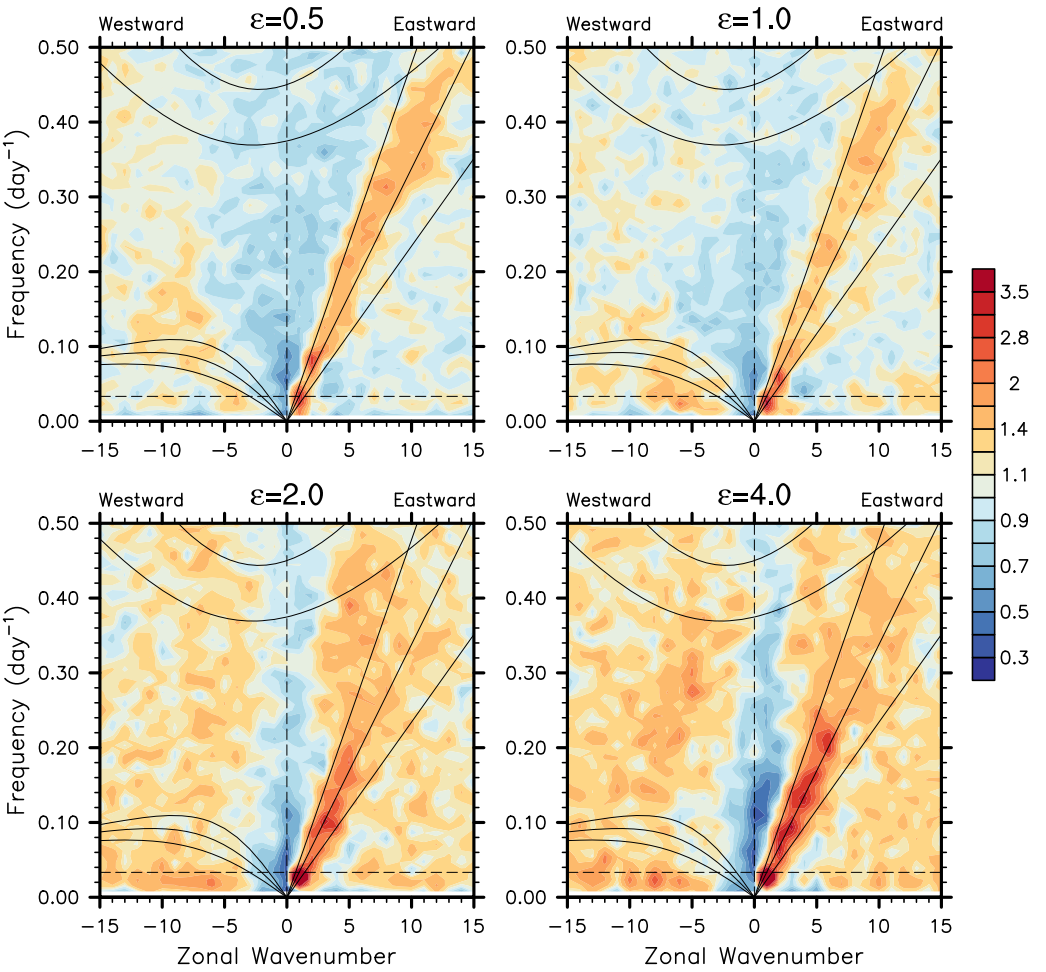

Figure 17. Equatorial wave number-frequency spectra of OLR symmetric across the equator, in CAM3.5 simulations with varying convective entrainment rate. Horizontal dashed line indicates a period of 30 days, and dispersion curves use 12, 25, and 50 m equivalent depths.

disappear. In rotating simulations with the conventional CAM, the level of MJO-like variability is found to depend on the convective entrainment rate, similar to the nonrotating aggregation. This is consistent with previous studies suggesting that the level of MJO activity in GCMs depends on a strong coupling between convection and tropospheric moisture [e.g., *Tokioka et al*., 1988; *Wang and Schlesinger*, 1999; *Lee et al*., 2003; *Zhang and Mu*, 2005; *Kim et al*., 2011].

These common features suggest that the MJO and nonrotating aggregation may share similar origins as moisture-based instabilities. Still, there remain significant differences in the details of their dynamics. The zonal scale of the MJO is 3–4 times the diameter of the aggregations, and has a zonally varying structure. These differences may result from beta-plane dynamics or interaction with the background state, but additional work is needed to fully understand them.

Some theories explain the MJO's large-scale convective envelope as a result of smaller-scale wave activity [e.g., *Majda and Biello*, 2004; *Yang and Ingersoll*, 2013]. However, these simulations show a tendency for convection to self-organize on scales approaching that of the MJO, under conditions without significant smaller-scale wave activity. Both convectively coupled equatorial waves and midlatitude synoptic-scale waves are absent in the nonrotating case, and thus play no role in supporting the large-scale convective envelopes. Instead, the simulated aggregation seems more consistent with a "modal" instability, in which diabatic feedbacks directly feed energy to larger scales [*Fuchs and Raymond*, 2005; *Raymond and Fuchs*, 2009; *Sobel and Maloney*, 2012].

Acknowledgments
The authors thank Bjorn Stevens and an anonymous reviewer for insightful comments that improved the manuscript. This work was supported by the National Science Foundation (USA) Science and Technology Center for Multi-Scale Modeling of Atmospheric Processes, managed by Colorado State University under cooperative agreement AGS-0425247. N.P.A. was supported by a NOAA Climate and Global Change postdoctoral fellowship. The model computations were carried out on the Stampede cluster at the University of Texas at Austin, supported by the National Science Foundation through XSEDE resources. The model output is archived and available by request.

References

Abbot, D. S. (2014), Resolved Snowball Earth Clouds, *J. Clim.*, *27*, 4391–4402.
Andersen, J. A., and Z. Kuang (2012), Moist static energy budget of MJO-like disturbances in the atmosphere of a zonally symmetric aqua-planet, *J. Clim.*, *25*, 2782–2804.
Araligidad, N. M., and E. D. Maloney (2008), Wind-driven latent heat flux and the intraseasonal oscillation, *Geophys. Res. Lett.*, *35*, L04815, doi:10.1029/2007GL032746.
Arnold, N. P., Z. Kuang, and E. Tziperman (2013), Enhanced MJO-like variability at high SST, *J. Clim.*, *26*, 988–1001.
Becker, T., and B. Stevens (2014), Climate and climate sensitivity to changing CO_2 on an idealized land planet, *J. Adv. Model. Earth Syst.*, *6*, 1205–1223, doi:10.1002/2014MS000369.
Benedict, J. J., and D. A. Randall (2007), Observed characteristics of the MJO relative to maximum rainfall, *J. Atmos. Sci.*, *64*, 2332–2354.
Benedict, J. J., and D. A. Randall (2009), Structure of the Madden-Julian Oscillation in the superparameterized CAM, *J. Atmos. Sci.*, *66*(11), 3277–3296.
Bony, S., and K. A. Emanuel (2005), On the role of moist processes in tropical intraseasonal variability: Cloud-radiation and moisture-convection feedbacks, *J. Atmos. Sci.*, *62*, 2770–2789.
Bony, S., et al. (2015), Clouds, circulation and climate sensitivity, *Nat. Geosci.*, *8*, 261–268.
Bretherton, C. S., M. E. Peters, and L. E. Back (2004), Relationships between water vapor path and precipitation over the tropical oceans, *J. Clim.*, *17*, 1517–1528.
Bretherton, C. S., P. N. Blossey, and M. Khairoutdinov (2005), An energy-balance analysis of deep convective self-aggregation above uniform SST, *J. Atmos. Sci.*, *62*, 4273–4292.
Craig, G. C., and J. M. Mack (2013), A coarsening model for self-organization of tropical convection, *J. Geophys. Res. Atmos.*, *118*, 8761–8769, doi:10.1002/jgrd.50674.
Crueger, T., and B. Stevens (2015), The effect of atmospheric radiative heating by clouds on the Madden-Julian Oscillation, *J. Adv. Model. Earth Syst.*, *7*, 854–864, doi:10.1002/2015MS000434.
Derbyshire, S., I. Beau, P. Bechtold, J.-Y. Grandpeix, J.-M. Piriou, J.-L. Redelsperger, and P. Soares (2004), Sensitivity of moist convection to environmental humidity, *Q. J. R. Meteorol. Soc.*, *130*(604), 3055–3079.
Emanuel, K., A. A. Wing, and E. M. Vincent (2014), Radiative-convective instability, *J. Adv. Model. Earth Syst.*, *6*, 75–90, doi:10.1002/2013MS000270.
Emanuel, K. A. (1987), An air-sea interaction model of intraseasonal oscillations in the tropics, *J. Atmos. Sci.*, *44*(16), 2324–2340.
Fuchs, Z., and D. J. Raymond (2002), Large-scale modes of a nonrotating atmosphere with water vapor and cloud-radiation feedbacks, *J. Atmos. Sci.*, *59*, 1669–1679.
Fuchs, Z., and D. J. Raymond (2005), Large-scale modes *of a rotating atmosphere with radiative-convective instability and WISHE, J. Atmos. Sci.*, *62*, 4084–4094.
Grabowski, W. W. (2001), Coupling cloud processes with the large-scale dynamics using the Cloud-Resolving Convection Parameterization (CRCP), *J. Atmos. Sci.*, *58*, 978–997.
Grabowski, W. W. (2003), MJO-like coherent structures: Sensitivity simulations using the Cloud-Resolving Convection Parameterization (CRCP), *J. Atmos. Sci.*, *60*, 847–864.
Grabowski, W. W. (2004), An improved framework for superparameterization, *J. Atmos. Sci.*, *61*(15), 1940–1952.
Grabowski, W. W., and M. W. Moncrieff (2004), Moisture-convection feedback in the tropics, *Q. J. R. Meteorol. Soc.*, *130*, 3081–3104.
Hannah, W. M., and E. D. Maloney (2014), The moist static energy budget in NCAR CAM5 hindcasts during DYNAMO, *J. Adv. Model. Earth Syst.*, *6*, 2754–2770, doi:10.1002/2013MS000272.
Held, I. M., M. Zhao, and B. Wyman (2007), Dynamic radiative convective equilibria using GCM column physics, *J. Atmos. Sci.*, *64*(228), 228–238.
Houze, R. A., and A. K. Betts (1981), Convection in GATE, *Rev. Geophys.*, *19*, 541–576.
Hung, M.-P., J.-L. Lin, W. Wang, D. Kim, T. Shinoda, and S. J. Weaver (2013), MJO and convectively coupled equatorial waves simulated by CMIP5 climate models, *J. Clim.*, *26*, 6185–6214.
Khairoutdinov, M. F., and K. Emanuel (2010), Aggregation of convection and the regulation of tropical climate, paper presented at 29th Conference on Hurricanes and Tropical Meteorology, Am. Meteorol. Soc., Tucson, Ariz.
Khairoutdinov, M. F., and D. A. Randall (2001), A cloud resolving model as a Cloud parameterization in the NCAR community climate system model: Preliminary results, *Geophys. Res. Lett.*, *28*, 3617–3620.
Khairoutdinov, M. F., and D. A. Randall (2003), Cloud resolving modeling of the ARM summer 1997 IOP: Model formulation, results, uncertainties, and sensitivities, *J. Atmos. Sci.*, *60*(4), 607–625.
Kiladis, G. N., M. C. Wheeler, P. T. Haertel, K. H. Straub, and P. E. Roundy (2009), Convectively coupled equatorial waves, *Rev. Geophys.*, *47*, RG2003, doi:10.1029/2008RG000266.
Kim, D., A. H. Sobel, and I.-S. Kang (2011), A mechanism denial study on the Madden-Julian Oscillation, *J. Adv. Model. Earth Syst.*, *3*, M12007, doi:10.1029/2011MS000081.
Lee, M.-I., I.-S. Kang, and B. Mapes (2003), Impacts of cumulus convection parameterization on aqua-planet AGCM simulations of tropical intraseasonal variability, *J. Meteorol. Soc. Jpn.*, *81*(5), 963–992.
Lin, J.-L., G. N. Kiladis, B. E. Mapes, K. M. Weickmann, K. R. Sperber, W. Lin, M. C. Wheeler, and S. D. Schubert (2006), Tropical intraseasonal variability in 14 IPCC AR4 climate models. Part I: Convective signals, *J. Clim.*, *19*, 2665–2690.
Madden, R. A., and P. R. Julian (1971), Detection of a 40-50 day oscillation in the zonal wind in the tropical pacific, *J. Atmos. Sci.*, *28*, 702–708.
Majda, A. J., and J. A. Biello (2004), A multiscale model for tropical intraseasonal oscillations, *Proc. Natl. Acad. Sci. U. S. A.*, *101*(14), 4736–4741.
Maloney, E. D. (2009), The moist static energy budget of a composite tropical intraseasonal oscillation in a climate model, *J. Clim.*, *22*(3), 711–729.
Mapes, B. (1993), Gregarious tropical convection, *J. Atmos. Sci.*, *50*(13), 2026–2037.
Mauritsen, T., and B. Stevens (2015), Missing iris effect as a possible cause of muted hydrological change and high climate sensitivity in models, *Nat. Geosci.*, *8*, 346–351.
Muller, C. J., and S. Bony (2015), What favors convective aggregation, and why?, *Geophys. Res. Lett.*, *42*, 5626–5634, doi:10.1002/2015GL064260.
Muller, C. J., and I. M. Held (2012), Detailed investigation of the self-aggregation of convection in cloud-resolving simulations, *J. Atmos. Sci.*, *69*, 2551–2565.

Neale, R. B., J. H. Richter, and M. Jochum (2008), The impact of convection on ENSO: From a delayed oscillator to a series of events, *J. Clim.*, *21*, 5904–5924.
Nilsson, J., and K. A. Emanuel (1999), Equilibrium atmospheres of a two-column radiative-convective model, *Q. J. R. Meteorol. Soc.*, *125*(558), 2239–2264.
Popke, D., B. Stevens, and A. Voigt (2013), Climate and climate change in a radiative-convective equilibrium version of ECHAM6, *J. Adv. Model. Earth Syst.*, *5*, 1–14, doi:10.1029/2012MS000191.
Raymond, D. J., and Z. Fuchs (2009), Moisture modes and the Madden-Julian Oscillation, *J. Clim.*, *22*(11), 3031–3046.
Raymond, D. J., and X. Zeng (2000), Instability and large-scale circulations in a two-column model of the tropical troposphere, *Q. J. R. Meteorol. Soc.*, *126*, 3117–3135.
Reed, K., B. Medeiros, J. Bacmeister, and P. Lauritzen (2015), Global radiative-convective equilibrium in the Community Atmosphere Model, version 5, *J. Atmos. Sci.*, *72*, 2183–2197, doi:10.1175/JAS-D-14-0268.1.
Richter, J. H., and P. J. Rasch (2008), Effects of convective momentum transport on the atmospheric circulation in the community atmosphere model, version 3, *J. Clim.*, *21*, 1487–1499.
Riley Dellaripa, E. M., and E. D. Maloney (2015), Analysis of MJO wind-flux feedbacks in the Indian Ocean using RAMA buoy observations, *J. Meteorol. Soc. Jpn.*, in press.
Shi, X., and C. S. Bretherton (2014), Large-scale character of an atmosphere in rotating radiative-convective equilibrium, *J. Adv. Model. Earth Syst.*, *6*, 616–629, doi:10.1002/2014MS000342.
Sobel, A., and E. Maloney (2012), An idealized semi-empirical framework for modeling the Madden-Julian Oscillation, *J. Atmos. Sci.*, *69*, 1691–1705.
Sobel, A. H., and C. S. Bretherton (2000), Modeling tropical precipitation in a single column, *J. Clim.*, *13*, 4378–4392.
Sobel, A. H., J. Nilsson, and L. M. Polvani (2001), The weak temperature gradient approximation and balanced tropical moisture waves, *J. Atmos. Sci.*, *58*, 3650–3665.
Sobel, A. H., G. Bellon, and J. Bacmeister (2007), Multiple equilibria in a single-column model of the tropical atmosphere, *Geophys. Res. Lett.*, *34*, L22804, doi:10.1029/2007GL031320.
Sobel, A. H., S. Wang, and D. Kim (2014), Moist static energy budget of the MJO during DYNAMO, *J. Atmos. Sci.*, *71*, 4276–4291.
Sugiyama, M. (2009), The moisture mode in the quasi-equilibrium tropical circulation model. Part I: Analysis based on the weak temperature gradient approximation, *J. Atmos. Sci.*, *66*, 1507–1523.
Tan, J., C. Jakob, W. B. Rossow, and G. Tselioudis (2015), Increases in tropical rainfall driven by changes in frequency of organized deep convection, *Nature*, *519*, 451–454.
Thayer-Calder, K., and D. A. Randall (2009), The role of convective moistening in the Madden-Julian Oscillation, *J. Atmos. Sci.*, *66*(11), 3297–3312.
Tobin, I., S. Bony, and R. Roca (2012), Observational evidence for relationships between the degree of aggregation of deep convection, water vapor, surface fluxes, and radiation, *J. Clim.*, *25*, 6885–6904.
Tobin, I., S. Bony, C. E. Holloway, J.-Y. Grandpeix, G. Seze, D. Coppin, S. J. Woolnough, and R. Roca (2013), Does convective aggregation need to be represented in cumulus parameterizations, *J. Adv. Model. Earth Syst.*, *5*, 692–703, doi:10.1002/jame.20047.
Tokioka, T., K. Yamazaki, A. Kitoh, and T. Ose (1988), The equatorial 30-60 day oscillation and the Arakawa-Schubert penetrative cumulus parameterization, *J. Meteorol. Soc. Jpn.*, *66*, 883–901.
Wang, W., and M. E. Schlesinger (1999), The dependence of convection parameterization of the tropical intraseasonal oscillation simulated by the UIUC 11-layer atmospheric GCM, *J. Clim.*, *12*, 1423–1457.
Wing, A. A., and T. W. Cronin (2015), Self-aggregation of convection in a long channel geometry, *Q. J. R. Meteorol. Soc.*, doi:10.1002/qj.2628, in press.
Wing, A. A., and K. A. Emanuel (2014), Physical mechanisms controlling self-aggregation of convection in idealized numerical modeling simulations, *J. Adv. Model. Earth Syst.*, *6*, 59–74, doi:10.1002/2013MS000269.
Yang, D., and A. P. Ingersoll (2013), Triggered convection, gravity waves, and the MJO: A shallow-water model, *J. Atmos. Sci.*, *70*, 2476–2486.
Zhang, C. (2005), Madden-Julian Oscillation, *Rev. Geophys.*, *46*, RG2003, doi:10.1029/2004RG000158.
Zhang, C., B. E. Mapes, and B. J. Soden (2003), Bimodality in tropical water vapour, *Q. J. R. Meteorol. Soc.*, *129*, 2847–2866.
Zhang, C., J. Gottschalck, E. D. Maloney, M. W. Moncrieff, F. Vitart, D. E. Waliser, B. Wang, and M. C. Wheeler (2013), Cracking the MJO nut, *Geophys. Res. Lett.*, *40*, 1223–1230, doi:10.1002/grl.50244.
Zhang, G. J., and N. A. McFarlane (1995), Sensitivity of climate simulations to the parameterization of cumulus convection in the Canadian climate centre general circulation model, *Atmos. Ocean*, *33*(3), 407–446.
Zhang, G. J., and M. Mu (2005), Simulation of the Madden-Julian Oscillation in the NCAR CCM3 using a revised Zhang-McFarlane convection parameterization scheme, *J. Clim.*, *18*, 4046–4064.